A Compact and Lightweight Aerial Manipulator for Installation and Retrieval of Sensors in the Environment

Salua Hamaza
Bristol Robotics Laboratory
Bristol, UK
s.hamaza@bristol.ac.uk

Ioannis Georgilas
University of Bath
Bath, UK
i.georgilas@bath.ac.uk

Andrew Conn
University of Bristol
Bristol, UK
a.conn@bristol.ac.uk

Guillermo Heredia
University of Seville
Seville, Spain
guiller@us.es

Aníbal Ollero
University of Seville
Seville, Spain
ollero@us.es

Thomas Richardson
University of Bristol
Bristol, UK
aetsr@bristol.ac.uk

Abstract

On-site inspection of large-scale infrastructure often involves high risks for the operators and therefore high costs. Despite several safety measures already in place to avoid accidents, an increasing concern has generated the need to remotely monitor hard-to-reach locations, for which the use of aerial robots able to interact with the environment has arisen. In this paper a novel approach to aerial manipulation is presented, where a lightweight compact manipulator with a single degree-of-freedom has been tailored for installation and retrieval of sensors in the environment. The proposed design integrates on-board sensing, a high-performance force controller on the manipulator, and a thrust-to-force mapping on the flight controller. Experimental results demonstrate the high reliability achieved during both installations and retrieval tasks on flat surfaces (e.g. a bridge wall) and cylindrical surfaces (e.g. tree trunks). A total number of 89 flight experiments were carried out in order to demonstrate the robustness and potential of the compact, bespoke aerial design.

1 Introduction

In the past few decades the increasing interest towards Unmanned Aerial Vehicles (UAVs) has sprouted a number of industrial and civil applications in which these platform are being used. Thanks to their unbounded workspace and inherent versatility, UAVs are deployed for a number of contact-less operations which exploit advanced on-board sensing, e.g. cameras, pressure sensors, flow sensors, LIDAR. Some example applications in which aerial vehicles are currently being used are civilian security, border security, fire and rescue, mountain rescue, distribution network monitoring, environmental monitoring, aerial photography, mapping and surveying. Despite proving very useful and successful, these applications are mostly limited to passive observation. However, huge potential lies in tasks that do require manipulation and physical interaction with the environment [Ruggiero et al., 2018].

Since 2009 [Bernard and Kondak, 2009] a new research area has risen, *aerial manipulation*, which considers endowing multicopters with mechanical devices to enable airborne manipulation tasks. Multicopters, e.g. quadcopters, hexacopters, octocopters, are Vertical Take-off and Landing (VTOL) aircraft that can hover, take off, and land vertically.

Figure 1: Example applications for UAMs include contact-based inspection of wind turbines, bridges, dams; or the installation of smoke detectors in forests for monitoring and fire prevention [Pexel, 2018].

This feature, together with the ability to fly stably at low speeds, greater manoeuvrability and greater payload capacity has made them particularly attractive for these type of applications. In its early stages, aerial manipulation main focus of interest laid in load transportation [Pounds et al., 2011b, Palunko et al., 2012] and grasping [Michael et al., 2011, Mellinger et al., 2013, Pounds et al., 2011a]. In more recent times, the scope has extended to the application of force in the environment for non-destructive testing (NDT) [Keemink et al., 2012, Fumagalli et al., 2014], assembly and disassembly [Jimenez-Cano et al., 2013, Augugliaro et al., 2013, Augugliaro et al., 2014], peg-in-hole [Korpela et al., 2013] or positioning [Kim et al., 2013, Suarez et al., 2017].

Unmanned Aerial Manipulators (UAMs) could be deployed to carry out inspection and maintenance operations in remote areas and hard-to-reach locations, performing tasks that are too risky for human operators and that require costly equipment. Some example scenarios where UAMs could be exploited are illustrated in Figure 1 and include the insulation of cracks on wind turbine blades, cleaning of clogged-up thermocouples on industrial chimneys, contact-based inspection of bridges and dams, installation and retrieval of smart sensors in wide-spread areas and infrastructure. Some of these example scenarios have been the case study of several investigations as part of multiple European funded projects in the past years, starting from [AIRobots, 2012] until most recently [ARCAS, 2015, AEROARMS, 2018, AEROWORKS, 2020].

In this work, the ability for an aerial manipulator to install and retrieve sensing devices in the environment is addressed. Remote sensing can bring several advantages as real-time monitoring of infrastructure and on-line surveying, therefore contributing towards hazard prevention or an accelerated response in case hazards occur. To carry out installation and retrieval tasks, the UAM should be capable of exerting a force in the environment by the use of an active tool that aids the positioning of such sensing devices. The interface between the gripper and the object held, or between the object and the environment may also pose limitations to the amount of force being applied by the manipulator: in case of interaction with delicate objects or surfaces, the use of a compliant approach becomes necessary.

1.1 Related Work

The state-of-the art in aerial manipulation mostly relates to solutions to perform grasping and transportation of an object with a UAM. The application of force on a surface is addressed in [Albers et al., 2010] for the first time, where a quadcopter is endowed with an additional propeller oriented horizontally to generate a normal force to a vertical

wall. No specific design for a manipulator is proposed but rather the addition of a cleaning tool/brush to use such force output for cleaning purposes. Results show that a mean force of 2.5 N is achieved over a period of 50 seconds. The major drawback of this solution relates to the limited flight time due to the presence of an extra rotor and the narrow scope of applications that can be achieved with the fixed tool (cleaning brush). In the recent works of [McArthur et al., 2018a, McArthur et al., 2018b] a tricopter UAV is equipped with an additional horizontal propeller for physical interaction with the environment. The "boomcopter" utilises the horizontal propeller propulsion to apply forces in hover state through a static end-effector. The scope for such design is the ability to position objects over flat vertical surfaces thanks to a press-to-release mechanism embedded in the end-effector.

In [Scholten et al., 2013] the ability to exert contact forces up to 3 N on a vertical wall is demonstrated with the use of a compact delta-robot mounted on the surrounding structure of the vehicle for gentle contact NDT purposes. In [Ryll et al., 2017] a novel approach is introduced with the use of tilt-rotor to apply a force over an inclined surface and be able to control independently both linear and angular accelerations of the UAV to counteract any opposing wrench. Similarly, in the work [Papachristos et al., 2014] the exertion of large forces for object manipulation is achieved through the use of a direct thrust-vectoring actuation on a tilt-rotor, with resulting forces over 20 N. Along the same lines, the work proposed by [Jiang and Voyles, 2013] shows a hexarotor performing a peg-in-hole task using a 6-DoFs manipulator inspired to a HEXA parallel robot. To generate a force on the interaction plane, i.e. X-Y plane of the aerial manipulator, the rotors' axes are tilted of a certain cant angle. This inclination distributes part of the aircraft thrust into a force normal to the wall for peg-in-hole purposes.

In [Bartelds et al., 2016b] the ability of the UAM to operate in more dynamical condition is introduced for the first time, with the case study of collision absorption thanks to a passively-compliant manipulator. It is demonstrated how high forces deriving from an impact are effectively absorbed by the on-board compliant manipulator and the resulting kinetic energy is stored within the spring element of the manipulator itself. In [Bartelds et al., 2016a] different control strategies for aerial manipulators handling highly dynamic physical interaction and aerial impacts are compared in simulation. In the author's previous work [Hamaza et al., 2018b, Hamaza et al., 2018a] a UAV equipped with a 2-DoF manipulator featuring active variable compliance can adjust the output force on a vertical wall by tuning the manipulator's controller gains. This allowed the UAM to tailor the force at the end-effector following a task-specific outcome. Another key result is the ability to apply rapid physical pulses over a surface for a period over 2 seconds with an average tapping frequency of 10 Hz. In [Wopereis et al., 2017] substantial forces up to 16 N are applied by an aerial vehicle equipped with a passive manipulator pitching at high angles against a flat vertical surface. This work mainly focusses on the control strategy over the pitch and yaw angles to guarantee stable contact for prolonged periods of time, however it has the limitation of a static contact point and limited end-effector motion due to its passive nature.

Inspired by the above efforts and in addition to the works seen in [McArthur et al., 2018a], [Wopereis et al., 2017] and [Bartelds et al., 2016b], this work presents a novel, lightweight design of an aerial manipulator capable of exerting considerable force to achieve such tasks as the installation and retrieval of smart sensors in different environments. The scope envisioned for the proposed aerial manipulator is the same as the one seen in [McArthur et al., 2018a], i.e. positioning of sensors in the environment, however the methodology differs in the following ways: we endorse the use of an autonomous active manipulator on-board a UAV (namely a UAM) to accomplish the task, as opposed to using a custom-made multicopter with tilted rotors or booms. Such a UAM combines the manipulator's force output with the vehicle motion to generate a force at the end-effector that can be adjusted in-flight. The active manipulator operates autonomously and its force output is independent of the UAV's. The main challenge tackled in this work is the ability to seamlessly combine the two systems in a single multi-variable platform to perform force-based operations airborne. The ability of retrieving such mounted sensors is also demonstrated with our setup for the first time, using a different end-effector design and different control inputs.

Force generation using the aircraft pitch is presented in [Wopereis et al., 2017]. Our work however, utilizes an actively compliant manipulator with a high-performance force controller and dedicated sensing which allows for real-time

control over the end-effector and force adjustments while in contact with the environment, as opposed to using a passive rod system. The active feature of the manipulator together with dedicated sensing are the key contributors to the robust and repeatable behaviour, which is successfully tested over flat and cylindrical surfaces. The aerial system as a whole is validated outdoors for the first time, and it is deployed to interact with tree trunks, as this poses a more realistic but challenging test scenario.

The paper's outline starts with the design considerations and concept that channeled the manufacturing of the UAM, in section 2. Then, the modelling and the solution of the kinematics and the dynamics are discussed in section 3. Section 4 introduces the control laws implemented in the aerial manipulator. In section 5 and 6, flight experiments carried out indoors and outdoors respectively are presented and discussed with an in-depth analysis of both the aircraft's and the manipulator's performance. Overall, the UAM behaviour is evaluated both on a single and multiple flights, and a statistical analysis is presented to validate the robustness and reliability of this approach. Finally, section 7 presents the conclusions drawn from this work.

2 Design of an Aerial Manipulator for Installation and Retrieval Operations

2.1 Design Considerations and Requirements

A recurrent approach found in the state-of-the-art when it comes to designing a manipulation system intended for aerial applications is to use serial types of manipulators, comprising n-joints providing n-Degrees-of-Freedom (DoFs) to the overall structure. However, despite the dexterity that a higher-DoF manipulator allows in terms of tasks that can be accomplished, there are several drawbacks that come with it. Primarily, a higher number of DoFs demands a higher number of actuators, therefore greater payload, higher control complexity, higher associated repair and maintenance costs, but also decreased manoeuvrability and battery life [Huber et al., 2013]. Hence, it is essential to limit the overall mass where possible and avoid redundancy while still devising the right tool for the job. Tasks that require limited object manipulation capabilities, for instance the exertion of a force normal to a surface for NDT, inspection by contact or the installation of sensors, can be achieved with a simple probe oriented towards the contact surface. Despite its simplicity, this type of approach provides a minimal, weight-efficient solution to the problem.

Hence, the first design requirement is posed to the manipulator's weight and the number of DoFs. A single-DoF manipulator is proposed, comprised of an active prismatic joint. To allow for a high force output within a compact lightweight solution, the use of rotation motors is favoured over linear motors: for the same force output, linear actuators are larger, heavier but also have less power efficiency than their rotational counterparts. Therefore, the use of a high-performance brushless DC motor paired with a rack and pinion transmission is utilized. Where possible the use of light sturdy materials is employed, such as polymer linear bearings (igus DryLin®), custom-made aluminum parts, and a rapid-prototyped ABS polymer housing for the rack and pinion mechanism.

Another design consideration relates to the distribution of mass and the overall UAM inertia: for aerial manipulators it is desirable to keep a compact design and move the end-effector contact point as close as possible to the aircraft Centre of Gravity (CoG). When manipulating an object, the added mass and gravitational force generate a momentum pivoting about the aerial platform that is directly proportional to the vector distance between the aircraft CoG and the contact point. In case the interaction takes place on the side of the vehicle, e.g. interaction with a wall, the vertical component of such a vector is crucial. Hence, reducing the vertical misalignment between the contact point and the CoG aids the overall stability. For this reason, the prismatic joint is oriented forward by means of an inclined support, making the tip of the rack tilted towards the centre of the platform.

Lastly, the presence of the manipulator and any moving masses act as disturbances on the aerial vehicle and tend to destabilize it. Therefore, it is desirable to reduce the relative motion between the manipulator and the aircraft and where possible group heavier components closer to the vehicle's CoG, minimizing the induced instability. This is frequently addressed in the literature with the use of one or multiple retractable arms, where the manipulator's configuration is kept compact and its CoG is close enough to the aircraft's CoG whilst not in operation. A compact design with minimal moving masses is not only beneficial to the aircraft stability, but also to its aerodynamics and battery life. In this sense, the proposed design with a single slider joint complies with these criteria more than other solutions with retractable arms, as no moving masses are present, except for the sliding rack (≈ 90 g).

2.2 Manipulation System Overview

The manipulation system consists of a single-DoF manipulator integrated with proximity and position sensors and communicating to the aerial platform via an on-board computer. The choice of a slider joint is made based on the requirement that the UAM needs to interact with the environment by applying a lateral force. The use of a passive slider was initially contemplated as a tool with which the UAV could have applied a force just by pitching towards an obstacle, propagating part of its thrust through the slider. However, the choice for the actuated prismatic joint was made to allow control over the position of the end-effector, and also to be able to control the force propagated by means of an additional motor.

2.3 Rack and Pinion Transmission

The slider is embodied by a rack and pinion transmission, driven by a high-performance force controller. The mechanical components are manufactured in metal as it brings several advantages in terms of precision, accuracy and lower wear coefficient. Moreover, as the pinion-rack mechanism is directly driven by the motor, it is the main responsible for the the power transmission. Aluminum material was chosen for the manufacturing of the components, for its low density and sturdiness. A double-sided pinion is coupled with the motor-shaft via a set screw. Two ball bearings are held in place at the extremities of the pinion to release the motor from any radial tension that might generate during interaction. A round rack gear slides within two polymer linear bearings, essential to ensure the adherence of the rack's teeth over the pinion during transmission. Figure 2 illustrates a cross section of the prismatic joint and its components. The module of the gears was chosen to be the lowest as possible to minimise the pinion's pitch diameter and provide

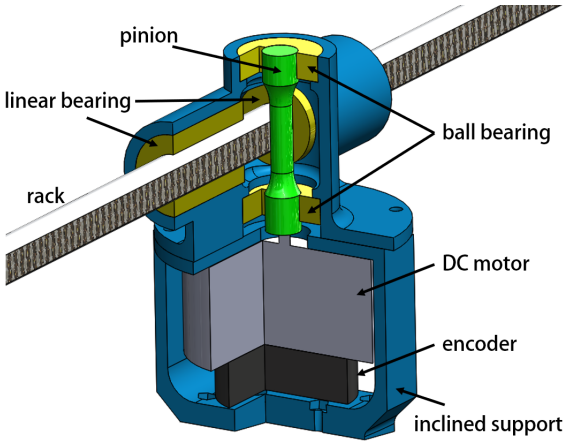

Figure 2: Cross section computer-aided-drawing (CAD) of the transmission mechanism and relevant components. A double-sided pinion (in green) drives the motion of the rack, whilst the encoder measures the relative position. A set of ball bearings and linear bearings (in yellow) assure accurate positioning of the pinion and the rack respectively, also distressing them from any lateral tension/momentum that may generate. The electronics and the distance sensor are not present in this figure.

a higher feed force to the end-effector. In fact, the feed force is:

$$F_{rack} = 2 \times \frac{T_{motor}}{d_p} = \frac{T_{motor}}{r_p} \tag{1}$$

where d_p and r_p are the pitch diameter and pitch radius of the pinion respectively. Rearranging Equation (1), the nominal torque T_{nom} required by the motor to generate an interaction force F_{rack} is derived. This torque must be less than the available stall torque to prevent overheating and to work within the reliable mechanical limits of the actuator itself.

To select the motor a rough estimate of the application force is necessary. According to the experimental results in [Bartelds et al., 2016b], in a scenario where a small-sized aerial manipulator is impacting rigidly with a wall the resulting forces may reach approximately 60 N. To be able to overcome different conditions with the proposed approach and provide a versatile solution that can be deployed with larger multi-rotors, the brushless DC motor which drives the pinion has a nominal torque $T_{nom} = 83.4$ mNm and stall torque $T_{stall} = 780$ mNm. The selected pinion has a pitch radius r_p of 2.5 mm, hence the nominal feed force generated by the selected motor is $F_{rack} = 33.3$ N, and the maximum force over a short period (e.g. 3 s) would be $F_{max} = T_{stall}/r_p = 312$ N.

2.4 Sensing

The manipulator is equipped with 2 high-performance sensors: an inductive MILE quadrature encoder on the actuator and a rangefinder located at the front of the aircraft. Both sensors have an update frequency of 1 kHz, allowing real-time control over the end-effector.

The encoder is directly coupled with the motor and measures the end-effector's relative position. The readings from the encoder are sent to the motor driver via a Quadrature Encoder Interface (QEI), then converted to metric measurements and updated in the *Forward kinematics* control block. Knowing the position of the slider joint and its relative displacement allows to have more accurate positioning over the end-effector and also to work within the available length of the rack, i.e. within its physical boundaries.

The rangefinder is mounted at the front of the vehicle and informs the manipulator's on-board computer of the relative position between the UAV and the obstacle ahead. The selected sensor uses the Time-of-Flight technology and it is preferred over ultrasound or infrared triangulation technologies as it allows for a much higher sampling frequency and long range measurements (over 12 metres). Similarly, laser technology was also discarded due to the bulkiness and high payload of commercially available laser scanners. The selected distance sensor is sized 35 x 29 x 18 mm, weighs 8 g and can measure distance within 14 m under different light conditions, making it suitable for both indoors and outdoors testing.

2.5 Grippers Design

Two different grippers are devised to address sensor installation and retrieval operations. For the placement task, the use of magnetic force is adopted to hold the sensor in place during flight and installation. The tip of the rack is equipped with a flat surface that resembles a lid. On top of it, a series of small Neodymium magnets are arrayed in such a way to prevent repulsion forces in between them. The same configuration is replicated on the outside of the sensor case, by mirroring the magnets. The adhesion force produced by the magnets F_{grip} must be enough to carry the sensor itself and overcome the forces generated by aerodynamic disturbances in flight, especially during take-off and in proximity of the wall:

$$F_{grip} \geq m_p g + F_{dist} \tag{2}$$

where m_p is the payload mass (e.g. sensor), g is the gravitational acceleration and F_{dist} is the force due to disturbances in flight, e.g. turbulence generated by the surrounding propellers during take-off, or due to the wall-effect. The computation of F_{grip} can be quite complex especially because it is dependent on the force due to disturbances, which is unknown and varies for each flight. To derive F_{grip} empirically some preliminary experiments were performed testing the reliability of different sizes of magnetic surface available. It was found that 2.5 cm^2 of magnetic surface provided a reliable adhesion between the gripper and a sensor of approximately 40 g, experiencing a failure rate below 1% spanned over 48 flights.

For retrieval tasks the gripper consists of a square hook with a threaded hole at one end. To secure the hook in place, a bolt is fastened along the hole, inside the rack. This design is selected as it facilitates the grasp, and for its manufacturing simplicity. To allow the hook to engage with the sensor a metal string was looped around the sensor case, acting as a support for the gripper and easing the pull. Figure 3 illustrates a close-up of both designs.

2.6 Integration with the Aerial Platform

2.6.1 Aerial Platform

The proposed 1-DoF manipulator design is manufactured and it is integrated on a small-sized aerial platform, namely the Lumenier QAV400 quadcopter (1.1 kg) powered by a 4s 2200 mAh battery (250 g). The main features of this aerial platform are listed in Table 1. The choice of a suitable platform for the specific application of installation and retrieval of sensor mainly focuses on the vehicle's available payload and flight time to carry out such operation. In the case of the proposed manipulator the total mass of mechanical and electronic components reaches 500 g, allowing the user to select a smaller sized platform that is safer to interact with, easier to fly and less costly to maintain and repair in case of failure. The choice of a commercially available platform is preferred over customized solutions to make aerial manipulation technologies more accessible to end-users. In fact, thanks to a modular design which can act as an add-on feature on an existing platform, users have the freedom to choose the most suitable vehicle and transit from UAV to UAM applications as they like.

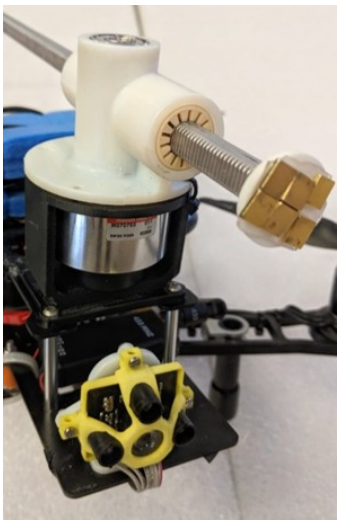

(a) Magnets array gripper.

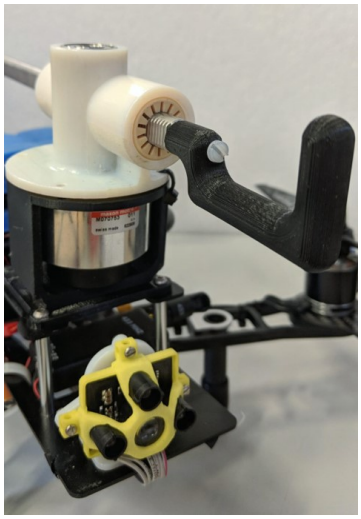

(b) Square hook gripper.

Figure 3: Gripper designs for (a) installation and (b) retrieval tasks.

2.6.2 UAM Configuration and Properties

The chosen platform allows to mount the developed manipulator on the top or bottom plate of the frame. The general rule when it comes to add masses on the aircraft is to position them as close as possible to the core of the aircraft to reduce the overall inertia of the aerial system. The "top" configuration is preferred as it generates a more favourable vehicle response: i.e. during aerial interaction the force generated at the tip of the end-effector induces a momentum on the aircraft that is anti-clockwise if the point of contact is above the vehicle CoG, causing the UAV to back off the wall. Viceversa, if the point of contact is below the vehicle's CoG, the induced clockwise momentum would cause the aircraft to tilt towards the wall, potentially leading to collision. Moreover, the available space on the bottom plate is dependent on the landing gear's geometry, and this places additional constraints to both the volume available and the range of motion of the manipulator.

The manipulator's components (motor board, computer, pinion-rack mechanism, sensing) are placed in such a way that the weight is distributed and symmetrical with respect to the vehicle's CoG. In this respect, the prismatic joint is mounted towards the front of the aircraft, while the battery is placed at the back to balance out the weight. Figure 4 illustrates some computer-aided design (CAD) drawings of the UAM from different views and the hardware layout.

In Table 2 the mass properties of the UAV and the UAM are presented. The centre of mass (CoM) coordinates are calculated based on a reference frame positioned in the centre of the vehicle with *z-axis* pointing upwards, *x* and *y* axes pointing towards the front and the side of the vehicle respectively. One can notice that the presence of the lightweight manipulator does not have much impact on the position of the CoG and on the moments of inertia along the main axes. In fact, the CoM of the system is only shifted by 1 cm along the *z-axis* and 2 cm along the *x*.

2.6.3 Hardware and Software Architecture

The on-board flight controller Pixhawk 4 uses the PX4 firmware and offers several flight modes: attitude, position, via-point and manual. During flight experiments, the UAV flies in position mode and is remotely controlled by a pilot via a FrSky Taranis X9D radio transmitter. The ground control software used to calibrate the vehicle's gains is

Table 1: System components and specifications.

QAV400 quadcopter		1-DoF manipulator	
Rotors	FX2216-9 1100kv	Motor	Maxon motor DC45 flat 50 Watt, 780 mNm stall torque
Propellers	8x5"	Motor controller	Maxon EPOS 24/3A Digital Controller 24 V, 3 A, 10 kHz sampling rate, 10 grams
Battery	LiPo 4s 2200 mAh	Battery	LiPo 4s 2200 mAh
Flight controller	Pixhawk 4 PX4 firmware	On-board computer	Raspberry Pi 3
Sensing	• 2 IMUs • Barometer • GPS	Sensing	• Terarager One distance sensor 0.2 - 14 m range, 1kHz sampling rate • MILE Maxon Encoder, 1024 CPT
Max. payload	0.8 kg	Max. payload	0.2 kg (1 kg if used stand-alone)
Flight time	10 minutes @0.5 kg	Operation time	max. available flight time or 2 hours if used stand-alone

Table 2: A comparison of the UAV and UAM mass properties: mass, centre of mass (CoM) coordinates and moments of inertia measured at the CoM.

	Aircraft only	Aircraft & manipulator	
m	1.35	1.85	$[kg]$
x_{CoM}	0.48	0.5	$[m]$
y_{CoM}	0	0	$[m]$
z_{CoM}	0.17	0.18	$[m]$
J_{xx}	0.03	0.03	$[kg \cdot m^2]$
J_{yy}	0.04	0.05	$[kg \cdot m^2]$
J_{zz}	0.07	0.07	$[kg \cdot m^2]$

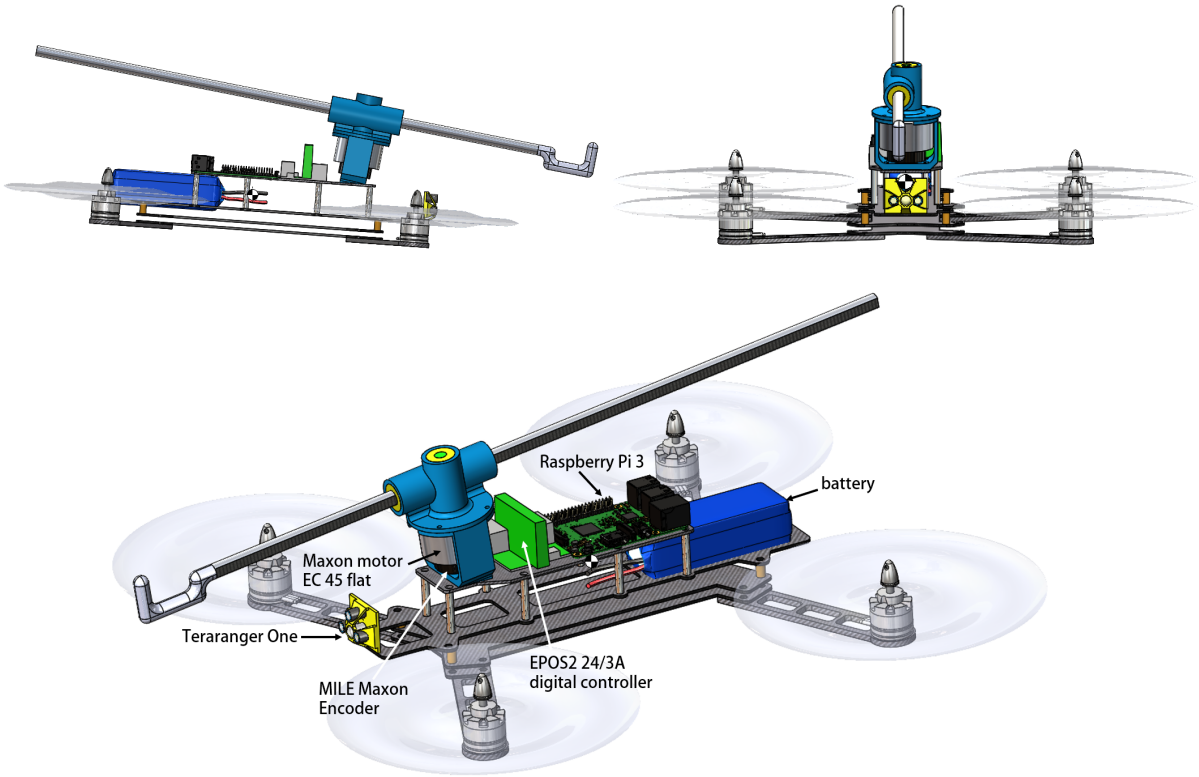

Figure 4: Computer-aided design drawings of the overall UAM system and components layout.

QGroundControl, which provides full flight control and vehicle setup for PX4 powered vehicles.

The manipulator's on-board computer is the Raspberry Pi 3 (1.4 GHz 64-bit quad-core ARM Cortex-A53 processor) with wireless LAN connectivity and logging capabilities. This processor is responsible for the UAM task management during operation and the manipulator's force control. A brushless DC motor "Maxon EC45 flat" with Hall sensor and MILE encoder actuates the motion of the pinion-rack mechanism through a Maxon EPOS2 24/3 motor digital controller board. This motor board is mainly selected as it offers a high sampling rate frequency for all its operation modes: 10 kHz in *current mode*, and 1 kHz in *position* and *velocity* mode. Such high performance allows to have real-time control over the manipulator, within a compact and lightweight solution (10 g). Lastly, a Teraranger One rangefinder is mounted at the front of the aircraft and sends distance information to the on-board computer.

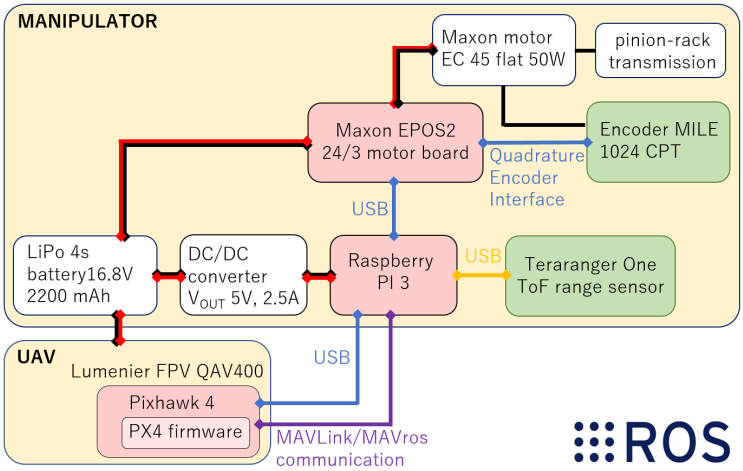

Figure 5: Hardware and software components and system architecture of the proposed UAM.

The software implementation is in Robotics Operating System (ROS). The main control node runs on the on-board Raspberry Pi and communicates with the UAV flight controller through a MAVLink/MAVros bridge. The overall system architecture is presented in Figure 5.

3 Modeling

The modelling of the proposed compliant manipulator is a key component when describing the behavior of the integrated system as a whole, namely the UAM. In this section the kinematics of the aerial manipulator is presented, the solution of which will be used in the *Control* section. The dynamic analysis of the coupled system is also presented.

3.1 Kinematics

Let us consider a quadcopter equipped with 1-DoF manipulator as depicted in Figure 6. By defining two coordinate frames, i.e. the ground frame $\mathcal{G}$ and the body-fixed frame $\mathcal{B}$, one is able to fully describe the motion of the aerial platform in space. However, in aerial manipulation two additional reference frames are adopted to account for the presence of the manipulator and the object to manipulate. The first, $\mathcal{M}$, is centred in the manipulator's CoG and the second, $\mathcal{E}$, is centred in the gripper/hand tool.

In this case, it is assumed that the manipulator centre of gravity coincides with the one of the aircraft. This assumption is based on the design choices discussed in the previous section and on the values found in Table 2: the proposed compact manipulator gathers its components at the base, shifting the manipulator's centre of mass towards the core of the platform where it is mounted. Also, while in operation the only moving part is the rack, which accounts for less than 5% of the UAM total mass. Therefore, thanks to the limited inertia generated by the rack's motion, no major impact is produced over the CoG position.

The reference frames used to solve the kinematic problem are displayed in Figure 6. Let us define three pose vectors: ${}^{\mathcal{G}}\boldsymbol{\pi}_{\mathcal{B}}$ describes the pose of the aircraft with respect to the ground frame, and vectors ${}^{\mathcal{G}}\boldsymbol{\pi}_{\mathcal{E}}$ and ${}^{\mathcal{B}}\boldsymbol{\pi}_{\mathcal{E}}$ describe the pose of the end-effector with respect to the ground and aircraft frames respectively. Vectors $\boldsymbol{\pi}$ consist of linear and angular terms about the x-y-z axes, as illustrated in Figure 6.

Due to the nature of quadcopters being underactuated systems the kinematics problem of the UAM is considered as a

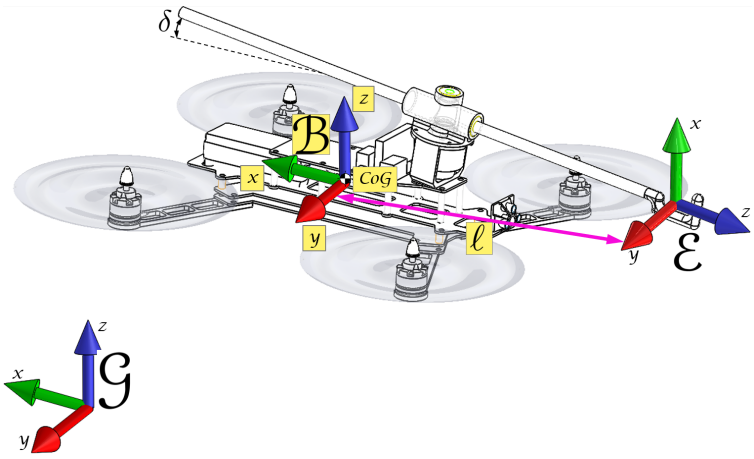

Figure 6: UAM reference frames.

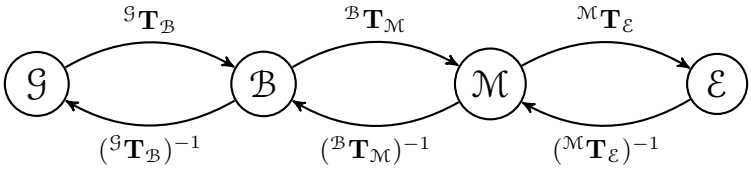

Figure 7: Schematic diagram representing the Forward and Inverse Kinematics problem for a generic UAM.

whole, as disturbances in the *roll-pitch-yaw* states affect the position of the end-effector. Hence the kinematic chain $\boldsymbol{\chi} = [\zeta_x\ \zeta_y\ \zeta_z\ \phi\ \theta\ \psi\ \mathbf{q}]^T$ describes the aerial system as a single, where $\boldsymbol{\chi}$ represents a $(6+1)$ dimension vector consisting of the aircraft linear and rotational terms (6 DoFs in space), and the scalar $\mathbf{q}$. The position of the end-effector with respect to the ground frame is represented by vector $^{\mathcal{G}}\boldsymbol{\pi}_{\mathcal{E}}$, which combines the multiplication of three homogeneous transformation matrices as follows: Each homogeneous transformation ($^{i}\mathbf{T}_{i+1}$) is a (4×4) matrix encompassing rotational and translation information of a space vector from frame i in superscript, to the resulting frame $i+1$ in subscript. Following the assumption that frames $\mathcal{B}$ and $\mathcal{M}$ coincide, the forward kinematics (FK) problem yields to:

$$^{\mathcal{G}}\boldsymbol{\pi}_{\mathcal{E}} = ^{\mathcal{G}}\boldsymbol{\pi}_{\mathcal{B}} + ^{\mathcal{B}}\mathbf{R}^{\mathcal{B}}_{\mathcal{E}}\boldsymbol{\pi}_{\mathcal{E}} = ^{\mathcal{G}}\mathbf{T}_{\mathcal{E}}(\boldsymbol{\chi}) = ^{\mathcal{G}}\mathbf{T}_{\mathcal{B}}(\zeta_x\ \zeta_y\ \zeta_z\ \phi\ \theta\ \psi)\ ^{\mathcal{B}}\mathbf{T}_{\mathcal{E}}(\mathbf{q}) \tag{3}$$

The position of the UAM depends on the relative position of the body-fix frame $^{\mathcal{G}}\boldsymbol{\pi}_{\mathcal{B}}$, and the end-effector $^{\mathcal{B}}\boldsymbol{\pi}_{\mathcal{E}}$. From Equation (3) it is now possible to solve the 1-DoF manipulator FK as a decoupled problem. Let us consider Figure 6: the UAV frame $\mathcal{B}$ has the $z_{\mathcal{B}}$ axis pointing upwards; frame $\mathcal{E}$ is rotated clockwise about $y_{\mathcal{B}}$ of an angle of $90° + \delta$, where δ takes into account the small inclination of the prismatic joint on the platform. Therefore, the end-effector is aligned with $z_{\mathcal{E}}$ and the distance between frames $\mathcal{B}$ and $\mathcal{E}$ along $z_{\mathcal{E}}$ varies with the motion of the slider, namely variable ℓ. With the above conditions, the Denavit-Hartenberg parameters are:

Table 3: Denavit-Hartenberg parameters for the proposed 1-DoF manipulator.

	i	a_{i-1}	α_{i-1}	d_i	θ_i
Link	1	0	$90° + \delta$	ℓ	0

which yields to:

$$^{\mathcal{B}}\mathbf{T}_{\mathcal{E}}(\mathbf{q}) = \begin{bmatrix} 1 & 0 & 0 & 0 \\ 0 & cos(90° + \delta) & -sin(90° + \delta) & -\ell sin(90° + \delta) \\ 0 & sin(90° + \delta) & cos(90° + \delta) & \ell cos(90° + \delta) \\ 0 & 0 & 0 & 1 \end{bmatrix} \tag{4}$$

The last column of the matrix displays the end-effector *x-y-z* coordinates with respect to frame $\mathcal{B}$. By knowing the extension of the rack, namely variable ℓ thanks to the on-board encoder, and the angle δ as part of the manipulator's design choices, the manipulator's FK problems is solved. The computation of the FK will then be used in the control block of the manipulator, as seen in the following section.

3.2 Dynamics

For a general multirotor, the thrust $\mathbf{T}(u)^i$ generated by each propeller *i*, is directed along the *z-axis* in the body-fixed frame $\mathcal{B}$. Similarly the torque $\boldsymbol{\tau}(u)^i$ generated by each rotor is about the same axis, $z_{\mathcal{B}}$. The total thrust vector $\mathbf{F}_a(u)$ is the summation of all $\mathbf{T}(u)^i$ terms measured in the ground frame $\mathcal{G}$. In a quadcopter, this is:

$$\mathbf{F}_a(u) = \sum_{i=1}^{4} \mathbf{T}(u)^i \tag{5}$$

$$\boldsymbol{\tau}_a(u) = \sum_{i=1}^{4} \boldsymbol{\tau}(u)^i + \Delta\mathbf{r}_i \times \mathbf{T}(u)^i \tag{6}$$

The above equations represent the force and torque of the aerial system generated by the rotors. Vector $\Delta\mathbf{r}_i \times \mathbf{T}(u)^i$ is the torque generated by the thrust vector $\mathbf{T}(u)^i$ about the centre of the vehicle, with arm $\Delta\mathbf{r}_i$. The aircraft lift force in Equation (5) must be enough to counteract the vehicle's gravitational force and other non-linear aerodynamic effects, e.g. gusts, turbulence due to the presence of obstacles (the wall-effect), and the presence of the manipulator. The equations of motion of the manipulation system can be derived using the Newton-Euler approach:

$$\begin{bmatrix} \mathbf{F}_m(\mathbf{q}, \dot{\mathbf{q}}, \ddot{\mathbf{q}}) \\ \boldsymbol{\tau}_m(\mathbf{q}, \dot{\mathbf{q}}, \ddot{\mathbf{q}}) \end{bmatrix} = \mathbf{M}(\mathbf{q})\ddot{\mathbf{q}} + \mathbf{C}(\mathbf{q}, \dot{\mathbf{q}})\dot{\mathbf{q}} + \mathbf{G}(\mathbf{q}) \tag{7}$$

where $\mathbf{M}$ is the generalised mass matrix comprising the inertial terms, matrix $\mathbf{C}(\mathbf{q}, \dot{\mathbf{q}})$ represents the Coriolis and centrifugal terms, and **G(q)** comprises of all gravitational terms acting on the manipulator. For a 1-DoF manipulation system, vectors $\mathbf{q}, \dot{\mathbf{q}}, \ddot{\mathbf{q}}$ are reduced to scalars, and likewise matrices $\mathbf{M}$, $\mathbf{C}(\mathbf{q}, \dot{\mathbf{q}})$ and $\mathbf{G}(\mathbf{q})$. In our case, the scalar quantity $\mathbf{q}$ consists of the prismatic joint variable ℓ.

As the manipulator dynamically interacts with an obstacle, the forces and torques generating at the end-effector propagate to the floating base. Hence, the coupled dynamics of the UAM system calculated with respect the the body-fixed frame $\mathcal{B}$ yield to:

$$\begin{bmatrix} \mathbf{F}_a(u) \\ \boldsymbol{\tau}_a(u) \end{bmatrix} + \begin{bmatrix} \mathbf{F}_m(\mathbf{q}, \dot{\mathbf{q}}, \ddot{\mathbf{q}}) \\ \boldsymbol{\tau}_m(\mathbf{q}, \dot{\mathbf{q}}, \ddot{\mathbf{q}}) \end{bmatrix} = \begin{bmatrix} m\,{}^{\mathcal{G}}\mathbf{R}_{\mathcal{B}}\mathbf{e_3} & \underline{\mathbf{0}} \\ \underline{\mathbf{0}} & \mathbf{I}(\mathbf{q}) \end{bmatrix} \begin{bmatrix} \dot{\mathbf{v}} \\ \dot{\boldsymbol{\omega}} \end{bmatrix} + \begin{bmatrix} \underline{\mathbf{0}} \\ \boldsymbol{\omega} \times \mathbf{I}(\mathbf{q})\boldsymbol{\omega} \end{bmatrix} \tag{8}$$

where m represents the UAM overall mass, multiplied by a (3×3) eye matrix $\mathbf{e_3}$ and rotation matrix ${}^{\mathcal{G}}\mathbf{R}_{\mathcal{B}}$; $\dot{\mathbf{v}}$ and $\dot{\boldsymbol{\omega}}$ are the linear and angular accelerations acting on the UAM, including the linear gravitational term $g = -9,81\ m/s$, $\underline{\mathbf{0}}$ is a (3×3) null matrix and $\mathbf{I}(\mathbf{q})$ is the inertia tensor about frame $\mathcal{B}$. The above equation describes the non-linear dynamics of the UAM and clearly shows how the propulsion and actuation systems of the vehicle and manipulator (left side of the equation) counterbalance the linear and angular dynamics of the system (on the right side).

4 Control

The control method used in this work focuses on the ability to install and collect small objects in the environment, such as smart sensing devices. Breaking down the task requirements leads to the ability to apply a compression or

tension force over a surface, hence the ability to control the interaction force is tackled. The presence of the active slider will allow to control the way the UAM approaches and eventually makes contact with the surface, by using it as a mechanical impedance tool on the environment. Another advantage of having an active manipulator as opposed to a passive one, is that it caters the UAV with an additional DoF and allows for a prompt, quicker response to the system as a whole. This is possible thanks to the simpler dynamics governing the manipulator and the embedded high-performance motor board of the joint.

4.1 Current-to-Force Mapping

The active prismatic joint is controlled in force through a PI current controller. Brushless DC motors present a constant relationship between the input current and the generated output torque, in accordance with the motor's specifications. For the selected motor the torque constant provided by the manufacturer is K_T = 33.5 mNm/A. The estimated manipulator's force $\mathbf{F}_m$ is proportional to the output torque (as seen in Equation (1)), hence introducing K_T yields to:

$$\mathbf{F}_m = c\, K_T r_p \varepsilon_e \varepsilon_m \tag{9}$$

where c is the input current, K_T is the torque constant and r_p is the pinion pitch radius. The above equation also factors in the efficiency loss in the actuator due to its internal friction ε_e, and the one due to the gearing in the pinion/rack transmission, ε_m. Both ε_e and ε_m are $<$1 and can be derived experimentally. Preliminary experiments are conducted to evaluate the manipulator force output in static condition, in particular the mapping between the current and the rack feed force. The experiments consist in generating a step signal in current on the motor, increasing by 100 mA every 5.5 seconds while the tip of the rack is in contact with a surface. The output force along the rack is then measured at the tip, via a 6 axis force/torque sensor.

Results are shown in Figures 8 and 9. Figure 8 shows the force and current signals plotted over time. The horizontal blue lines show the mean value of the force data, whilst the grey vertical lines display where an abrupt change in the mean value of the force is met. These changes are in conjunction with the current steps, despite a small delay at the beginning of each line due to the time shift between the current signal sent by the motor and sensed by the force sensor. It can be observed that the minimum current required to overcome the static friction of the system and sense a force of about 1.6 N is 100 mA. Figure 9 shows a line connecting the mean values in force (yellow line) and the linear regression of those (orange line). The equation displays the relationship between force and current found experimentally and can be compared to Equation (9) where the product of coefficients $K_T r_p \epsilon_e \epsilon_m$ can be grouped in single constant, namely the slope of the linear fit. The range of operation of the motor current used in the later flight experiments is below 600 mA; even so the current-to-force linear relationship shown in Figure 8 is expected to hold for higher values.

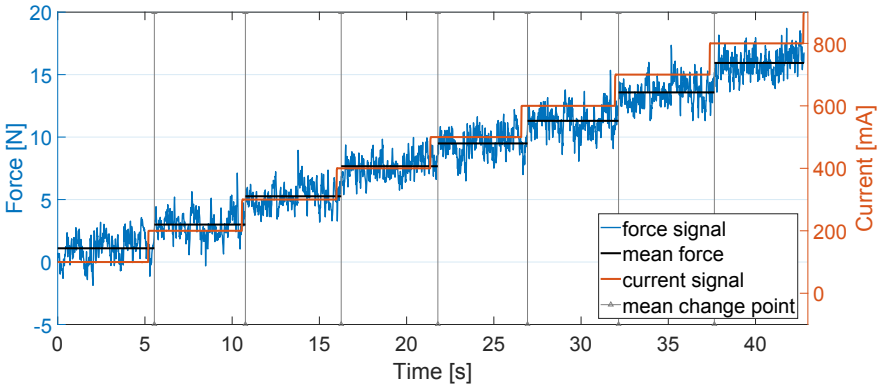

Figure 8: Evaluation of the manipulator feed force in static condition: mapping between the input motor current (right axis) and resulting output force measured via a force/torque sensor (left axis). The relationship between the two variables is linear.

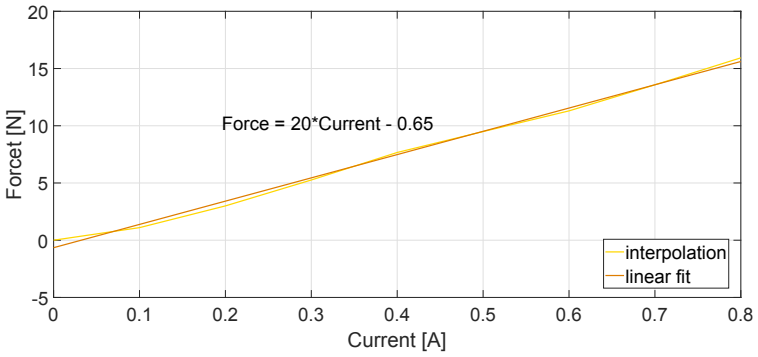

Figure 9: Interpolation of the mean force values of the current-to-force mapping of the previous figure and a 1st-order fitting.

4.2 Pitch-to-Force Mapping

Besides the action of the manipulator, the aerial vehicle contributes to the large part of the exertion of force on the surface. Let us consider the UAV in contact with the surface by mean of a rigid rod and pitching forwards at an angle of θ. As the rod lies on the y-z plane, the force $\mathbf{F}_a(u)_{z\ axis}$ generated by the vehicle and propagated through the stick will lie on the same plane, as illustrated in Figure 10. This force represents the static horizontal component of the vehicle's thrust, along the z axis as follows:

$$\mathbf{F}_a(u)_{z\ axis} \propto mgtan(\theta) \tag{10}$$

The above equation shows how the force sensed at the target surface is proportional to the vehicle weight and pitch angle in the static case, however this does not take into account the motion of the vehicle. The dynamics involved in the interaction contribute towards the total contact force, for example the vehicle speed of approach, the impact with the surface, and disturbances caused by the turbulence in the proximity with the wall. To maintain contact with the surface for prolonged periods of time, the vehicle must increase the thrust vector $\mathbf{F}_a(u)$ to counteract an equal and opposite reaction force and moment generating at the surface. This way, the UAV is able to cancel out such reaction forces and reach the equilibrium.

To have an accurate estimate of the UAV's contribution towards the contact force, several calibration experiments have been performed with the same setup as the one used later on in flight experiments. Within this calibration, the manipulator's controller is disabled and the rod rigidly attached on the vehicle to mimic the conditions of Figure 10. The quadcopter approaches the vertical wall at a constant speed of 0.2 m/s flying in *position* mode. Once contact is established with the surface, the pitch angle progressively increases and the force output at the surface is measured

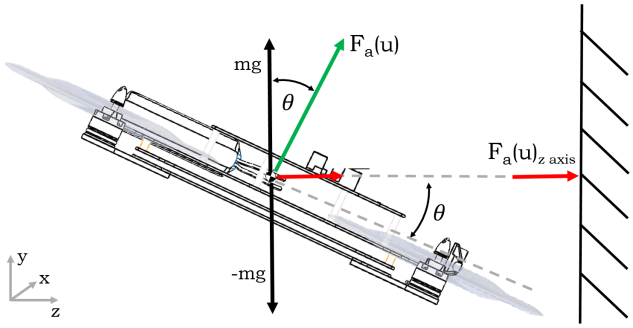

Figure 10: Sketch of the UAV pushing against a vertical surface via a rigid stick. The vehicle generates a force on the target surface that is proportional to its weight and pitch angle, in static conditions.

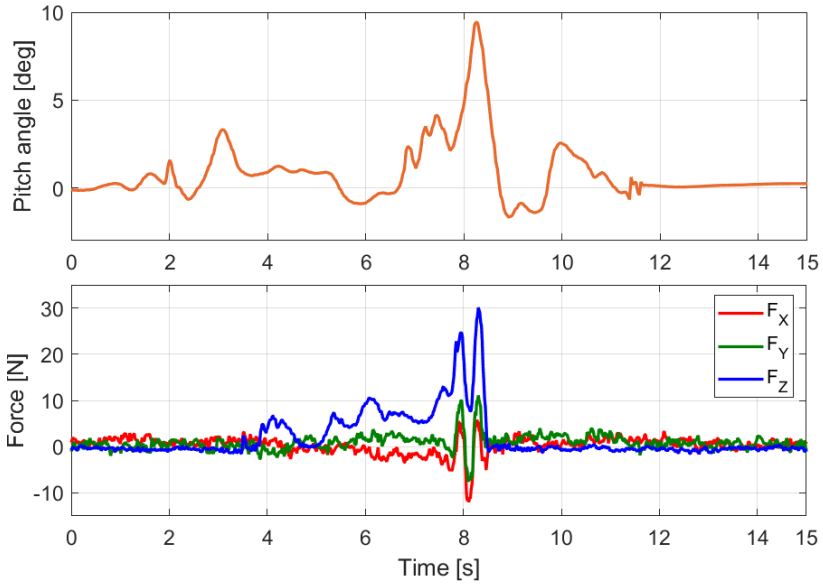

Figure 11: Sample flight experiment to evaluate the pitch-to-force ratio of the UAM.

by a 6-axis Force/Torque sensor mounted on the wall. On average, the pitch angles reached during the calibration experiments range between $5°$ to $17°$. Results of a sample test are displayed in Figure 11.

It can be seen that at about t = 4 s the UAV is in contact with the wall and a positive force is sensed. As the pitch progressively rises to $10°$, the force measured reaches 30 N along the *z-axis* (the axis normal to the surface), while minor lateral forces generate as well along the *x-y* axes. It was found that with angles higher than $5°$ the throttle value on the UAV would rise more quickly, generating a sudden change in the force output measured at the wall and additional perturbations in the yaw angle. This is also visible in the figure, as forces along *x-y* axes are more prominent as the pitch rises beyond $5°$. Although the Figure above is just a sample of several experiments performed to describe the pitch-to-force mapping, this trend was consistent throughout multiple data-sets, with a force on average above 25 N at $10°$ and a standard deviation of $\pm$ 4.3 N.

4.3 Force Control

Let us consider the control problem of a mass m (UAV) attached to a spring element (manipulator) with stiffness k_m. The final goal is to be able to control the UAV and maintain a desired contact force $\mathbf{F}_{des}$ with the environment, which is the force acting in the spring element $\mathbf{F}_m = k_m x$. Hence, the equation that describes the physical system is:

$$\begin{aligned}\mathbf{F} &= m\ddot{x} + k_m x + \mathbf{F}_{dist} \\ &= m k_m^{-1} \ddot{\mathbf{F}}_m + \mathbf{F}_m + \mathbf{F}_{dist} \\ &= m k_m^{-1} [\ddot{\mathbf{F}}_{des} + k_{vf}\dot{e}_f + k_{pf} e_f] + \mathbf{F}_m + \mathbf{F}_{dist}\end{aligned} \tag{11}$$

where $\mathbf{F}_{dist}$ is the force due to disturbances, e.g. friction in the manipulator gearing, $e_f = \mathbf{F}_{des} - \mathbf{F}_m$ is the force error between the desired force $\mathbf{F}_{des}$ and the contact force $\mathbf{F}_m$. The above equation considers a close-loop system where the force output on the environment $\mathbf{F}_m$ is sensed and fed back, leading to the control law:

$$\ddot{e}_f + k_{df}\dot{e}_f + k_{pf} e_f = 0 \tag{12}$$

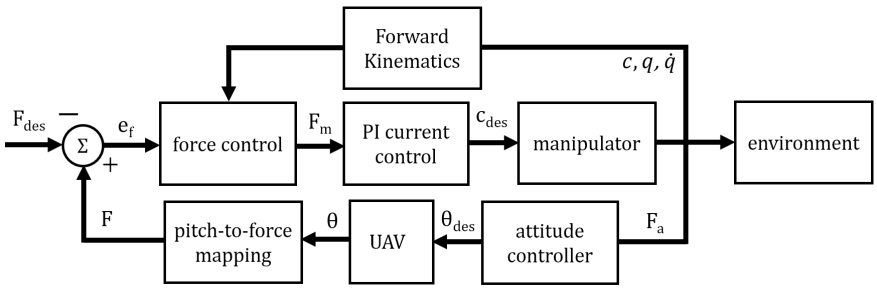

Figure 12: Block diagram of the UAM control architecture.

Following the method proposed by [Craig, 2005], one can assume that while the end-effector is in contact with the environment, its dynamics do not change over time. Accordingly, the contact forces do not change over time in static conditions, except for some small oscillations present in the system, e.g. noise. Therefore, the time derivatives terms of the force can be set as zero: $\ddot{\mathbf{F}}_{des} = \dot{\mathbf{F}}_{des} = \dot{\mathbf{F}}_{m} = 0$. Hence rearranging Equation (11) for an open-loop system and including $\mathbf{F}_{des}$ yields to:

$$\mathbf{F} = mk_{pf}k_{m}^{-1}e_{f} + \mathbf{F}_{des} \tag{13}$$

The UAM control architecture is illustrated in the block diagram of Figure 12 and follows a decentralized approach [Jimenez-Cano et al., 2013, Ruggiero et al., 2018] to take advantage of the high performance embedded motor controller of the manipulator.
Starting from the left side, the desired force $\mathbf{F}_{des}$ is subtracted to $\mathbf{F}$, generating an error e_f that is the input of the proportional control law seen in Equation (13). The force demand is then converted into a desired current value c_{des} and inputted in the motor controller board Maxon EPOS2 24/3 that runs on a Proportional-Integral (PI) control loop. The motor board actuates the slider joint and moves the manipulator towards the target, i.e. the environment block. The position, velocity and current states at the end-effector are measured and sent to the forward kinematics block. The force exerted by the UAV pitching motion is estimated and corrected by adjusting the desired pitch angle θ_{des}, the resulting angle is then converted to force using the mapping seen in the previous section.

The *task manager* and main force controller run on the on-board Raspberry Pi 3. The internal PI current control runs on the Maxon EPOS2 24/3 digital board operating at 10 kHz. The motor states $q, \dot{q}$ are measured by the digital encoder; the vehicle relative position is measured by the distance-sensor. Both sets of data are processed by the Raspberry Pi which computes the forward kinematics and the mapping between force and current, as discussed in section [4.1].

5 Indoor Experiments

This section presents the validation of the novel lightweight aerial manipulator's design in an indoor setting. The proposed mechanical design, combined with dedicated sensing and the control laws previously discussed is tested as a single multi-variable system and it is aimed at facilitating the installation and retrieval of smart sensors in hard-to-reach locations, without the use of additional supporting equipment, or scaffolding around the structure itself. A total of 48 flight experiments are conducted to validate installation and retrieval operations indoors over a flat vertical surface. An interaction with a vertical surface already encompasses the vast majority of targeted environments where the aerial manipulator could be deployed, such as a bridge wall, a dam, a wind-turbine blade with low-curvature profile, the side of a building, and so on.

5.1 Experiment Outline

Each experiment is staged as follows: at first, the pilot flies the quadcopter in *position mode* towards the target whilst the on-board flight controller corrects any positioning error on the vehicle (approach stage). The use of a VICON motion capture system is employed to correct the pose estimator on the flight controller. The UAV then approaches the contact surface, i.e. a flat wooden panel, and once the vehicle is hovering in close proximity, the manipulator's task manager reads the vehicle angular states and the distance sensor measurements. If the values are within the accepted threshold, the manipulator autonomously triggers (interaction stage). On top of these requirements, an upper layer is implemented in the task manager which relies on the pilot confirming a "go-ahead" input before triggering. This input is implemented on one of the radio control switches and allows the pilot to visually check if the operation is safe to conduct. It was found that this additional safety measure allowed a more robust and repeatable behaviour over the numerous experiments carried out. In the "settling" stage, the manipulator has completed the installation/retrieval task, the rack retracts and the UAV is homed.

During the interaction, force measurements are collected by a 6-axis Force/Torque sensor (Robotiq FT 300) mounted on the target surface. The sensor sampling rate is 100 Hz and provides readings up to $\pm$ 300 N on the force and $\pm$ 30 Nm on the moment. It is important to highlight that the force information from the sensor is used as a ground-truth measurement during the indoors experiments, and not as a way to close the force control loop. Lastly, all force data presented in this section follow the convention seen in Figure 6, namely F_z is the force normal to the wall and it is the one to be controlled.

5.2 Sensor Installation Indoors

The objective of these experiments is to validate the bespoke manipulator design and control laws for installation tasks that require a considerable exchange of force with the environment. The challenge faced in these experiments is to seamlessly combine the force output of the manipulator and of the vehicle in a stable and safe way with a slow force build-up, and to be able to use this force to place a sensor securely onto a flat surface. The second challenge is to control the direction of the force to guarantee a correct installation; if the lateral component of the force is too high due to undesired yaw on the UAV, the end-effector may slip over the target inducing a sudden rotation in the system, leading to failure and potential damage to the UAV. This will be further discussed in the following section "Outdoor Experiments".

A total of 33 experiments were performed to validate installation tasks indoors. In Figure 13 results of a single sample flight during a successful installation are illustrated, with a focus on the range information of the distance sensor, the force generated by the manipulator, the end-effector position, and the UAV angular states. Figure 14 displays the force measured by the Force/Torque sensor mounted at the target during the same experiment.

To begin with, the UAV approaches the target surface at a constant speed of 0.2 m/s. To install the sensor, a sinusoidal signal is used to slowly protrude the end-effector outwards. The low current that drives the end-effector outwards allows for a gentle, compliant touch with the surface and establishes a safe contact. The sensor case is provided with adhesive pads on the *wall* side to allow it to stick on the target surface. Once in contact, the force is progressively increased to ensure a sufficient adhesion of the pads and therefore secure the object in place. The manipulator's force output reaches about 5 N during the installation, whilst the highest proportion of the force output is generated by the UAV itself progressively pitching against the surface. Prior to contact, a few oscillations in pitch occur due to the turbulence in the wall proximity. However, in the majority of the cases these disturbances did not affect the positive outcome of the installation and were overall below $\pm$ 5°.

In this particular experiment, a maximum pitch angle of 16.2° is reached and a high compression force up to -46 N is sensed at the target (see Figure 14). From the previous section, we recall that the force output is also dependant

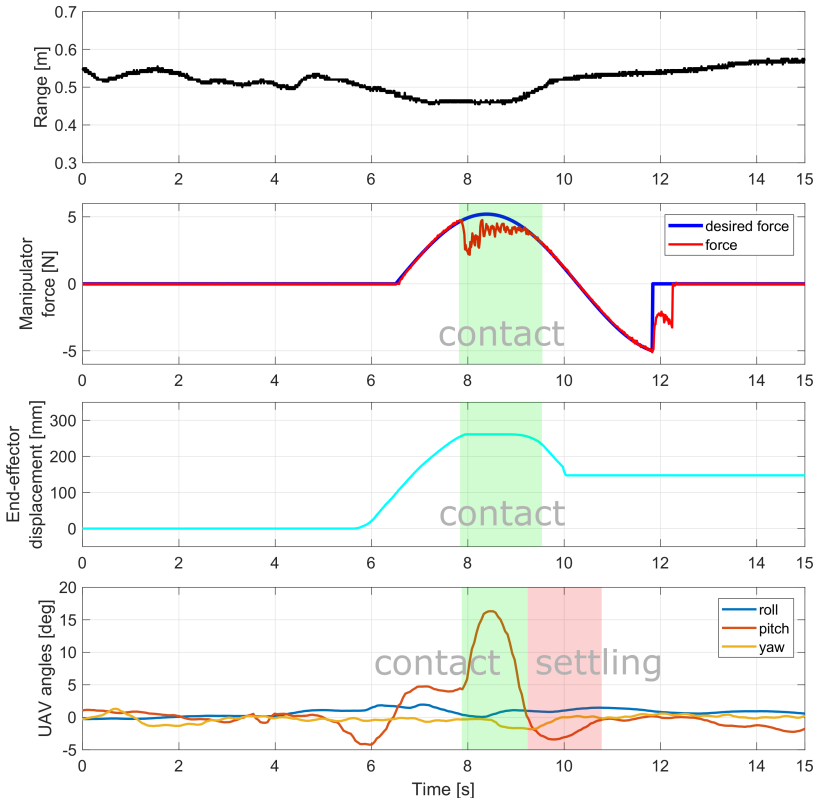

Figure 13: Sensor installation indoors - data collected by the on-board Raspberry Pi 3. From top to bottom: range information by the distance sensor mounted at the front of the UAV; compression force exerted by the manipulator, end-effector position and UAV angular states. The highlighted boxes delimit areas of interest, namely the contact stage and the UAV settling stage after interaction.

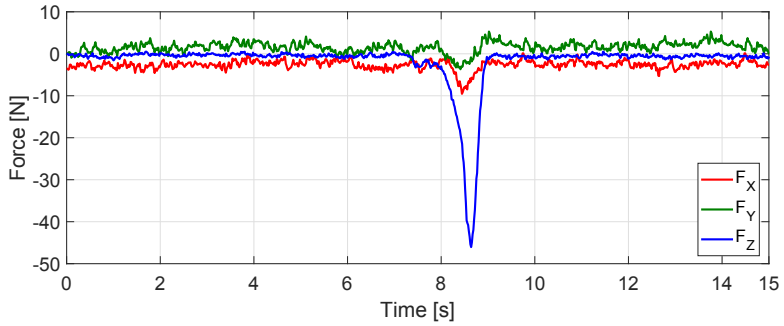

Figure 14: Sensor installation indoors - ground-truth measurements of the forces by a 6-axis force/torque sensor.

on the vehicle dynamic response when approaching the surface, i.e. speed of approach and momentum generated during the impact. These factors contribute towards higher forces resulting from each installation task. At $t \approx 9s$, the manipulator begins to retract and simultaneously the UAV's pitch angle is decreased, moving the force output F_z towards zero. At the beginning of the vehicle "settling stage", a minor overshoot below the zero is sensed in pitch as the UAV renters the hover state following the detachment with the target surface.

The range measurements present no drastic change throughout the dataset as the UAM approaches, installs the sensor, and homes back. This is mainly because the vehicle positioning is corrected by the flight controller in close-loop control with the motion tracking system, allowing it to adjust any sudden undesired movement due to, for example, an induced momentum. As the UAV hovers in proximity of the wall at the start of the operation, the distance from the target oscillates around 0.5 ± 0.05 m, while it starts to diverge more noticeably as the rod retracts, causing a

rapid change in the distribution of masses on the vehicle. In Figure 15 a time-lapse sequence of a single successful installation indoors is displayed.

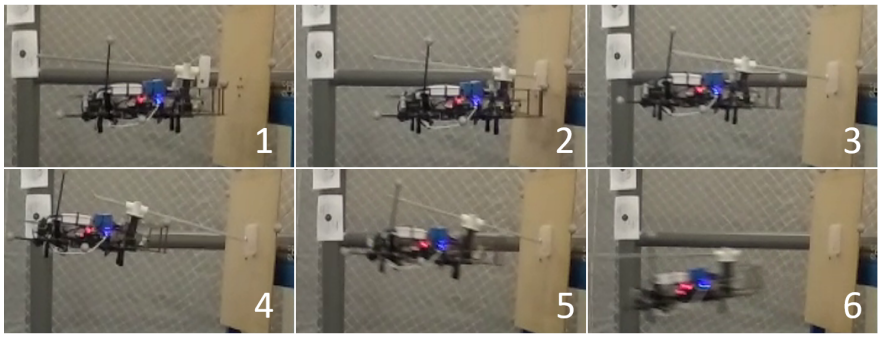

Figure 15: Time-lapse sequence of an aerial installation of sensor indoors.

Table 4: A summary of the statistics following indoors installation experiments and insights on the mean and standard deviation values of multiple variables averaged throughout the set of 33 experiments.

Sensor Installation Indoors		
Total experiments	33	
Success rate	84.8%	
$AVG\ \mu_{roll} \pm \sigma_{roll}$	0.90 $\pm$ 0.45	[deg]
$AVG\ \mu_{pitch} \pm \sigma_{pitch}$	6.91 $\pm$ 7.93	[deg]
$AVG\ \mu_{yaw} \pm \sigma_{yaw}$	0.44 $\pm$ 0.62	[deg]
$AVG\ \mu_{force} \pm \sigma_{force}$	-27.3 $\pm$ 8.94	[N]
max. force	-47.05	[N]

In Table 4 a summary of the statistical evaluation of the overall performance of the UAM during installations indoors is illustrated, along with the success rate over the 33 attempts. Overall, 28 out of 33 installations are successful, with a failure rate of about 15%. Failure was associated with the UAM failing to secure the pad on the target surface and this was mostly due to a positioning error in *yaw*, which prevented the system from reaching the necessary *pitch* to guarantee enough adhesion of the sensor's pads on the wall.

For each flight the mean value μ and standard deviation σ for roll, pitch, yaw angles and the force output sensed at the wall are computed for both the *contact* and *settling* stages. Subsequently, the values of each variable are averaged over the total number of flights and presented in Table 4 as $AVG\ \mu$ and $AVG\ \sigma$ respectively. The table provides an idea of the overall trend of the vehicle stability and force output measured in the experiments. The average μ values are below 1° along roll and yaw angles and likewise the respective standard deviation σ, meaning that the angular disturbances of the aircraft during interaction are quite low and that the vehicle is stable. The pitch angle presents a higher mean value and standard deviation as we would expect. The average force measured during indoor installation tasks is 27 N, while the maximum force reached in the experiments is -47 N. The standard deviation σ_{force} shows that the difference in the force output is dependant on the dynamic response of the UAV during contact and the momentum gained before the impact.

5.3 Sensor Retrieval Indoors

A total of 15 experiments was performed to validate indoor aerial retrieval. Within these experiments, the ability to engage with and detach an object placed on a vertical wall is validated. The challenge with retrievals is to guarantee a stable hover in close proximity to the wall, which allows the end-effector to hook the sensor in a robust way and

therefore initialize the pulling motion to collect it.

To start with, the UAV flies close to the target surface, with the end-effector extended outwards. The sensor case is already placed on the flat panel by mean of adhesive pads. As the UAM establishes contact with the surface, the manipulator is initially kept passive to ensure a compliant contact with the sensor case. As the end-tool engages with the sensor, the rack automatically retracts exerting a constant force in the opposite direction and pulling the sensor away from its environment. The manipulator autonomous behaviours is triggered when an error in position and force is sensed at the end-effector. Results of a single sample retrieval flight are illustrated in Figures 16, 17.

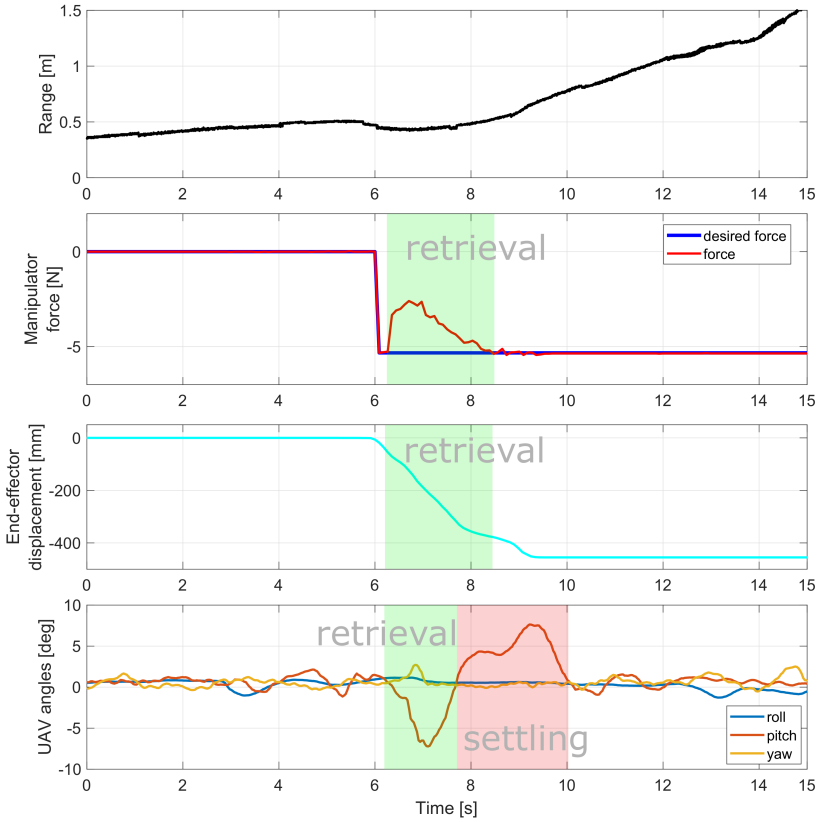

Figure 16: Sensor retrieval indoors - data collected by the on-board Raspberry Pi 3. From top to bottom: range information by the distance sensor mounted at the front of the UAV; pulling force exerted by the manipulator, end-effector position and UAV angular states. The highlighted boxes delimit areas of interest, namely the contact stage and the UAV settling stage after interaction.

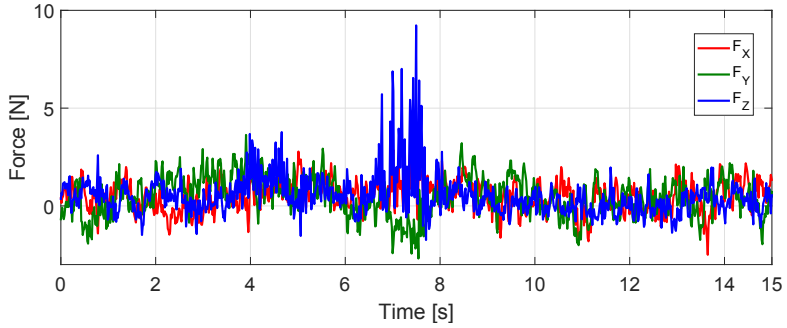

Figure 17: Sensor retrieval indoors - ground-truth measurements of the forces by a 6-axis force/torque sensor.

It can be observed that between $5.2 < t < 7.5$ s the manipulator is overcoming the adherence force of the pads to retrieve the object causing an error in the force (red line). In response to this, the force controller increases the pull

and successfully collects the object. The pulling motion is also visible in Figure 17 where a positive tension force is measured by the force/torque sensor of about 5 N on average.

During the "retrieve" stage the UAV also contributes towards the pulling force by pitching upwards, generating a nose-up pitching moment. Once the sensor is retrieved and the rack fully retracted, some oscillations generate in the vehicle in an attempt to regain the hover state. This is similar to what was seen in the previous section where perturbations in pitch are caused by the sudden detachment from the wall and rapid change in the inertia of the system. A time-lapse sequence of frames captured during a single retrieval task is displayed in Figure 18.

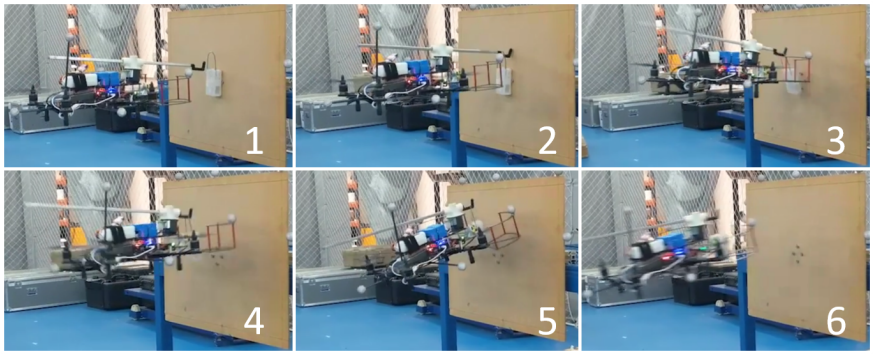

Figure 18: Time-lapse sequence of an aerial retrieval of sensor indoors.

Table 5: A summary of the statistics following indoors retrieval experiments and insights on the mean and standard deviation values of multiple variables averaged throughout the set of 15 experiments.

Sensor Retrieval Indoors		
Total experiments	15	
Success rate	100%	
$AVG\ \mu_{roll} \pm \sigma_{roll}$	0.64 ± 0.24	[deg]
$AVG\ \mu_{pitch} \pm \sigma_{pitch}$	1.40 ± 5.27	[deg]
$AVG\ \mu_{yaw} \pm \sigma_{yaw}$	0.49 ± 0.56	[deg]
$AVG\ \mu_{force} \pm \sigma_{force}$	6.16 ± 2.04	[N]
max. force	9.23	[N]

In Table 5 a summary of the statistical evaluation of the UAM performance during retrievals indoors is illustrated. Overall, 15 out of 15 retrieval experiments were found to be successful. The values $AVG\ \mu$ and $AVG\ \sigma$ are the mean and standard deviation of the angular states and the force averaged over the total number of flights. The average pitch angle, namely $AVG\ \mu_{pitch}$, measured during retrieval operations is below 10° and shows that a lower force is necessary to pull the sensor away from the surface. From the table we can derive that the angular disturbances in *roll-pitch-yaw* are generally lower than those found in the installation experiments. This is attributed to the nature of the operation itself which requires a less dynamic response and proves overall less challenging to handle from the UAV perspective. Likewise, the maximum force measured by the force/torque sensor is 9.23 N showing that the UAM dynamics involved in these tasks are less demanding than those seen in the previous section.

6 Outdoor Experiments

A total of 41 outdoors experiments were performed outdoors to test the proposed UAM in more complex conditions. Typically the majority of aerial applications for UAMs includes the interaction with vertical or tilted surfaces of different materials, however the ability to perform installations on more challenging surfaces is tested to further validate

the robustness of our approach. In particular, cylindrical irregular surfaces such as tree trunks are chosen for the following outdoors experiments, as they resemble one of the most challenging targets with whom UAMs could operate due to their irregular shape and texture. The experiments are performed on a range of several trees with the purpose to install and retrieve small sensors, such as smoke detectors, to prevent forest fires or to achieve real-time monitoring and surveying.
Flying outside brings additional challenges such as accurate position sensing and the presence of unknown obstacles that can generate turbulence over the vehicle. The purpose of these tests was therefore to demonstrate if placement and retrieval is in essence feasible and to identify the best approach to take in order to improve reliability.

6.1 Experiment Outline

The experimental setup used for outdoors experiments is similar to to the one seen previously, except for the lack of motion capture system reading the UAV states, and the Force/Torque sensor measuring the contact force on the tree trunks. The lack of the VICON tracker reduces the accuracy in the vehicle's pose estimation, which only relies on the use of an on-board GPS. Due to the partial occlusion of the GPS signal in the proximity of tree branches and other obstacles, the flight controller pose estimator experiences a higher level of noise as opposed to open-field flying. An additional precaution taken in this respect was to lower the flight controller gains to have less aggressive flight manoeuvres.

6.2 Sensor Installation Outdoors

In Figure 19 results of a single sample flight during a successful installation are illustrated. For outdoors experiments, the *current* input used to extend and retract the end-effector was generally lower when compared to the indoors flights. This was chosen so as to increase the compliance of the end-effector when in contact with the tree and to have a less aggressive behaviour. Moreover, the sinusoidal signal in force has a shorter period compared to the previous section. This is because the duration of the contact is reduced and the force output is tailored for outdoors experiments to perform a safer interaction and account for sudden disturbances in the position estimator. Once contact is established, the UAV progressively increases its pitch to generate a good adhesion on the object, then flies backwards after a successful placement.

Results are illustrated in Figure 19. The second figure from the top shows the manipulator's force during the task: contact with the tree occurs at $t = 7$ s, where the impact of the object on the target surface generates a force error in the controller. During this time, the manipulator is still extending (see third figure). As the object is installed and the UAV retrieves the loiter state, disturbances in *pitch* and *yaw* generate, as seen in the bottom figure (settling area).

A general trend experienced in outdoors experiments is the longer settling time needed by the UAV to retrieve the hover state and higher disturbances sensed in *pitch* and *yaw*. As previously discussed, one of the major factors that plays a role in pose estimation is the use of GPS over the VICON motion tracker, which affects the positioning accuracy. Another potential source for a longer settling time and higher angular disturbances is the presence of gusts and other obstacles that induce turbulence, e.g. surrounding trees, branches. Despite these factors, the "settling stage" had minimal effect on the overall success rate of the outdoors trials, with the main cause for failure assigned to an undesired yaw during contact that induced slippage at the end-effector. The undesired yaw generated a lateral force at the end-effector causing it to move out of the interaction plane$y$-z, slipping over the trunk and therefore not generating enough adhesion on the sensor adhesive pads.

In Table 6 a summary of the statistical evaluation of the overall performance of the UAM during installations outdoors is illustrated, along with successful rate throughout the 23 attempts. Overall, 18 out of 23 installations were successful, with a failure rate of about 21%. As experienced in the indoor setting, failure was attributed to an undesired yaw which

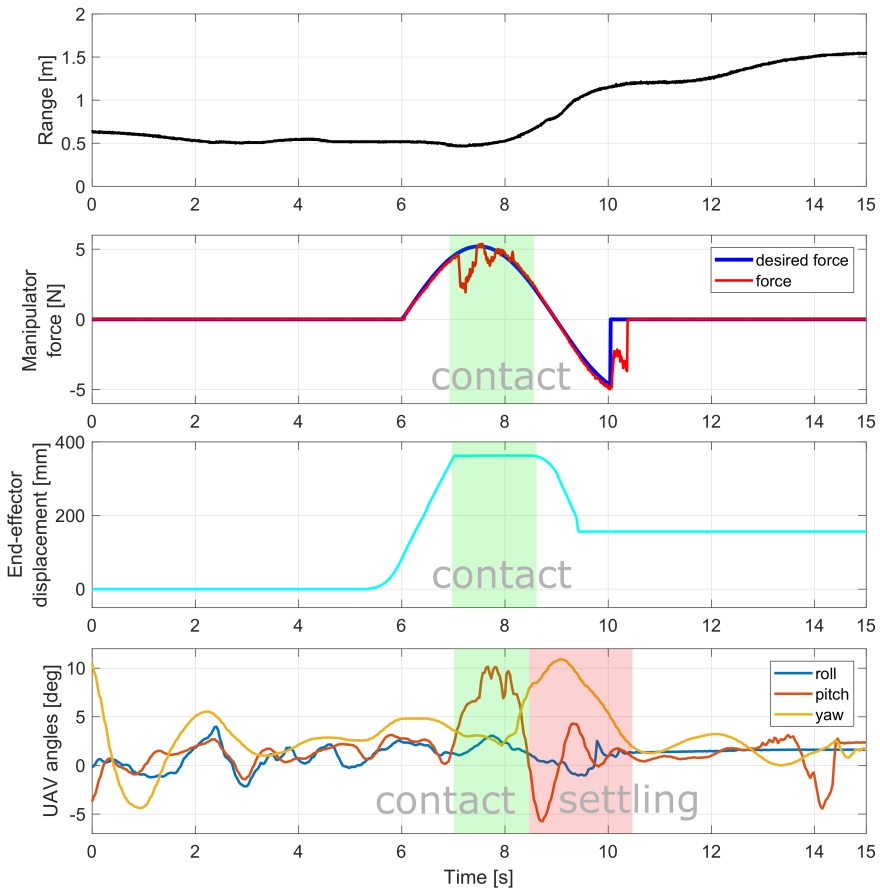

Figure 19: Sensor installation outdoors - data collected by the on-board Raspberry Pi 3. From top to bottom: range information by the distance sensor mounted at the front of the UAV; pushing force exerted by the manipulator, rack displacement and UAV angular states.

caused slippage of the end-effector on the target surface, even more so as the target is a cylindrical surface. The table here presented follows the same notation as the ones seen above, where $AVG\ \mu$ and $AVG\ \sigma$ show the averaged mean and standard deviation values for multiple variables and give an idea of the overall trend of the vehicle stability measured in the experiments, validating the repeatability and robustness of our approach.

It can be seen that the larger variations in *yaw* experienced during outdoors experiments are recorded within the mean μ_{yaw} and standard deviation σ_{yaw}, as these values appear to be larger than in previous cases. The pitch angles reached during installation are lower than those seen in the indoor setting, and this reflects in lower mean and standard deviation values. This is because, as previously discussed, the time of contact with the tree was reduced with respect to indoor trials, hence the pitch "build-up" is also lower. Overall, the pitch angle reached during outdoors installations ranges between [5°,12°]. A time-lapse sequence of frames captured during a single installation task outdoors is displayed in Figure 20.

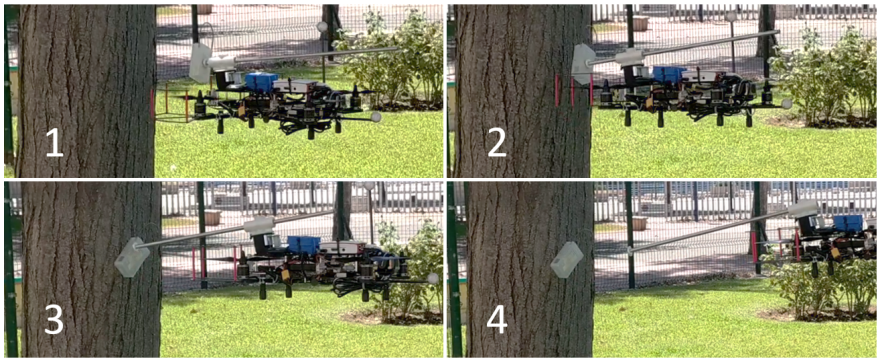

Figure 20: Time-lapse sequence of an aerial installation of sensor outdoors.

Table 6: A summary of the statistics following outdoors installation experiments and insights on the mean and standard deviation values of multiple variables averaged throughout the set of 23 experiments.

Sensor Installation Outdoors		
Total experiments	23	
Success rate	78.2%	
$\boldsymbol{\mu_{roll} \pm \sigma_{roll}}$	1.07 ± 1.27	[deg]
$\boldsymbol{\mu_{pitch} \pm \sigma_{pitch}}$	3.57 ± 5.02	[deg]
$\boldsymbol{\mu_{yaw} \pm \sigma_{yaw}}$	4.60 ± 2.90	[deg]
estimated avg. force	-22	[N]

6.3 Sensor Retrieval Outdoors

Outdoor retrieval experiments were carried in the same way as indoors. Results are shown in Figure 21. In general, the same challenges as the indoor setting were present, however the GPS-based flight made long-term stable hovering in the proximity of the sensor more challenging outdoors as opposed to indoors. Also, the UAV settling time was also found to be longer, as with outdoor installations. Often, the pitch angle oscillates between [-10°,10°] after retrieving the object from the wall, with oscillations also present in yaw. As seen before for the indoor retrieval, the angular disturbances generate from the detachment with the tree as well as the end-effector retracting motion, causing a sudden change in the momentum of the vehicle. Despite these oscillations, the overall success rate in outdoors retrievals is 100% over 18 experiments performed, demonstrating a higher repeatability than outdoors installations. This is a result that was also found in the indoor setting: the nature of the retrieval task itself leads to a higher robustness during interaction, as it requires a less aggressive and less dynamic behaviour on the flight controller to complete the task. A time-lapse sequence of frames captured during a single installation task outdoors is displayed in Figure 22.

Table 7: A summary of the statistics following outdoors retrieval experiments and insights on the mean and standard deviation values of multiple variables averaged throughout the set of 18 experiments.

Sensor Retrieval Outdoors		
Total experiments	18	
Success rate	100%	
$\boldsymbol{\mu_{roll} \pm \sigma_{roll}}$	0.32 ± 0.27	[deg]
$\boldsymbol{\mu_{pitch} \pm \sigma_{pitch}}$	1.37 ± 4.42	[deg]
$\boldsymbol{\mu_{yaw} \pm \sigma_{yaw}}$	0.45 ± 3.95	[deg]
estimated avg. force	6.4	[N]

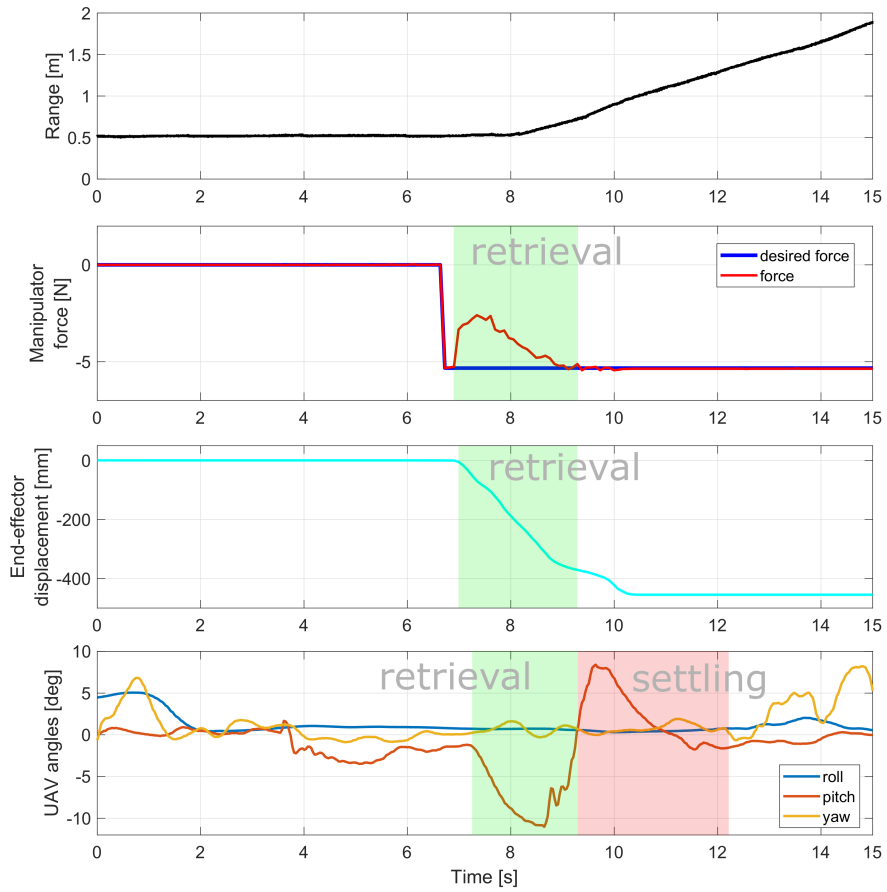

Figure 21: Sensor retrieval outdoors - data collected by the on-board Raspberry Pi 3. From top to bottom: range information by the distance sensor mounted at the front of the UAV; pulling force exerted by the manipulator, rack displacement and UAV angular states.

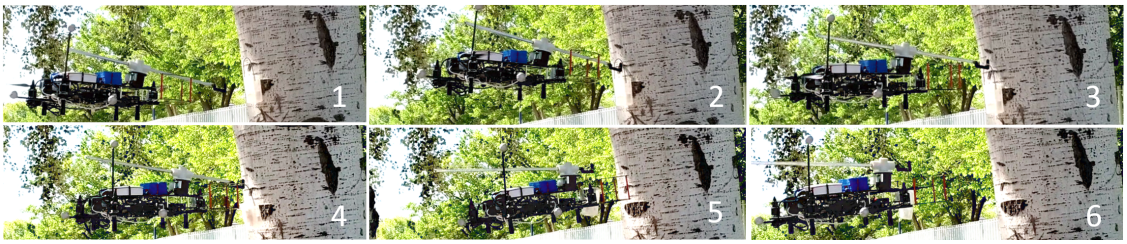

Figure 22: Time-lapse sequence of an aerial installation of sensor outdoors.

In Table 7 a summary of the statistical evaluation of the overall performance of the UAM during retrieval tasks outdoors is illustrated, along with successful rate throughout the 18 attempts. Overall, the angular disturbances were significantly less than those in installations outdoors. Disturbances in the *pitch* and *yaw* are still present, due to the turbulence caused by the propellers moving close to branches and the trunk. However, such disturbances did not affect the positive outcome of the retrieval operations, and all attempts were successful.

To conclude, outdoors experiments demonstrated the feasibility and robustness of the proposed approach for both placement and retrieval tasks. The conclusions drawn from these experiments showed that a stable hover and a more compliant behaviour were key elements to succeed in the outdoor setting. In particular, the demanded force output of the aerial system was lowered, as it was the one of the manipulator. The flight controller gains were also lowered to decrease the likelihood of any aggressive behaviour of the vehicle in the proximity of obstacles. Lower *pitch*

angles were reached to compensate for the less accurate GPS-based pose estimation, generating a lower force output and lower pitch build-up. The combination of all these factors proved that outdoor operations were possible and repeatable, where a total of 41 data-sets were produced.

7 Conclusions

Safety is of paramount importance when it comes to the inspection of bridges, dams, wind turbines and other large-scale infrastructure. Where human operators are involved, both time and costs can be significant. Putting in additional safety measures to allow access to remote monitoring sites can require supporting structures, on-site scaffolding or other special equipment often incurring in extra time and costs associated to these operations. Unmanned aerial manipulators capable of planting smart sensors in hard-to-reach locations or wide-spread areas could therefore significantly reduce the time and costs required to inspect such locations.

To address such tasks, a small-sized UAV equipped with a lightweight, compact manipulator is presented in this paper detailing the mechanical design, sensing and the integration with the aerial platform together with the modeling and control of this novel aerial manipulator. The strength of this design lies in the simplicity of the transmission mechanism and its minimal weight which make it a suitable modular solution for on-site inspection with different aerial platforms. The proposed UAM is ideal for force-driven aerial tasks such as the placement and retrieval of objects, non-destructive testing and contact-based inspection. A total of 89 data-sets was produced to demonstrate the reliability and robustness of our approach and the following lessons have been learned:

- devising a manipulator that is adequate for the task is a key design requirement and it unfolds in several sub-requirements such as minimizing the payload, addressing the weight distribution and optimising the configuration/integration on the aerial vehicle. These are all essential elements that improve the dynamic response of the flying robot whilst interacting with a surface;

- distance sensing on the UAM is beneficial and it can be used to automate the operation, however it is of limited use during the interaction and the settling stages. Other forms of visual sensing or event-based cameras could be incorporated to further improve sensory feedback on-board and refine the autonomous behaviour;

- real-time force control has proved to be a reliable approach for the specific application of object placement and retrieval and we believe the validation in the outdoor setting has shown its versatility and potential for other force-induced tasks;

- force sensing is essential to inform the platform on how the interaction is affecting the system's variables, and it allows to achieve closed-loop control over the force;

- indoor experiments demonstrate the effectiveness of the approach in a monitored environment, with accurate pose estimation over the vehicle. Results showed that the UAM is capable of dynamically adjust its angular states whilst in contact with the surface and to combine the force output generated by the active manipulator and by the UAV's pitching motion. This allows the UAM to generate a force-to-weight ratio of 130% on average during installations, with a maximum force of 230% its weight;

- outdoor experiments demonstrated good reliability of the proposed UAM in more challenging conditions and with less accurate pose estimation of the vehicle. Lower gains on the flight controller ensured a more gentle and compliant approach and helped to handle the uncertainty of the outdoor setting, for example GPS signal occlusion. Lower force outputs were demanded on the aerial system, resulting in a less aggressive dynamic response. This ensured a safer interaction with the tree.

- the proposed UAM has the capability to interact with with different targeted environments, such as flat vertical surfaces and irregular cylindrical surfaces, demonstrating repeatable outcomes and its robustness as a single multi-variable system;

To conclude, the work presented in this paper aims at demonstrating the capabilities of the proposed lightweight compliant manipulator for force-driven aerial tasks such as the installation and retrieval of smart sensors in the environment and it lays the foundations towards more dexterous aerial manipulation tasks. Further work will address the refinement of the flight controller with the use of Model Predictive Control methods (MPC) in order to minimize the angular disturbances of the vehicle during interaction and achieve a successful rate during installation greater than 90%. Also, the design of new grippers will be evaluated to stretch the number of applications that can be achieved with the proposed manipulator, together with additional sensory feedback solutions.

Acknowledgments

The authors would like to acknowledge the support provided by the members of the Robotics, Vision and Control Group at University of Seville, Spain. In particular Manuel Fernandez, Pedro Sanchez and Rafael Salmoral for their help during flight experiments.

References

AEROARMS (2018). AEROARMS Project. https://aeroarms-project.eu/.

AEROWORKS (2020). AEROWORKS Project. http://www.aeroworks2020.eu/.

AIRobots (2012). Airobots project. http://airobots.ing.unibo.it/.

Albers, A., Trautmann, S., Howard, T., Nguyen, T. A., Frietsch, M., and Sauter, C. (2010). Semi-autonomous flying robot for physical interaction with environment. In *Robotics Automation and Mechatronics (RAM), 2010 IEEE Conference on*, pages 441–446. IEEE.

ARCAS (2015). ARCAS Project. http://www.arcas-project.eu.

Augugliaro, F., Lupashin, S., Hamer, M., Male, C., Hehn, M., Mueller, M. W., Willmann, J. S., Gramazio, F., Kohler, M., and D'Andrea, R. (2014). The flight assembled architecture installation: Cooperative construction with flying machines. *Control Systems, IEEE*, 34(4):46–64.

Augugliaro, F., Mirjan, A., Gramazio, F., Kohler, M., and D'Andrea, R. (2013). Building tensile structures with flying machines. In *2013 IEEE/RSJ International Conference on Intelligent Robots and Systems*, pages 3487–3492. IEEE.

Bartelds, J., Wopereis, H. W., Stramigioli, S., and Fumagalli, M. (2016a). A comparison of control approaches for aerial manipulators handling physical impacts. In *2016 24th Mediterranean Conference on Control and Automation (MED)*, pages 646–652. IEEE.

Bartelds, T., Capra, A., Hamaza, S., Stramigioli, S., and Fumagalli, M. (2016b). Compliant aerial manipulators: Toward a new generation of aerial robotic workers. *IEEE Robotics and Automation Letters*, pages 477–483.

Bernard, M. and Kondak, K. (2009). Generic slung load transportation system using small size helicopters. In *Robotics and Automation, 2009. ICRA'09. IEEE International Conference on*, pages 3258–3264. IEEE.

Craig, J. J. (2005). *Introduction to robotics: mechanics and control*, volume 3. Pearson/Prentice Hall Upper Saddle River, NJ, USA:.

Fumagalli, M., Naldi, R., Macchelli, A., Forte, F., Keemink, A. Q., Stramigioli, S., Carloni, R., and Marconi, L. (2014). Developing an aerial manipulator prototype: Physical interaction with the environment. *Robotics & Automation Magazine, IEEE*, 21:41–50.

Hamaza, S., Georgilas, I., and Richardson, T. (2018a). An adaptive-compliance manipulator for contact-based aerial applications. In *2018 IEEE/ASME International Conference on Advanced Intelligent Mechatronics (AIM)*, pages 730–735. IEEE.

Hamaza, S., Georgilas, I., and Richardson, T. (2018b). Towards an adaptive-compliance aerial manipulator for contact-based interaction. In *2018 IEEE/RSJ International Conference on Intelligent Robots and Systems (IROS)*, page in press. IEEE.

Huber, F., Kondak, K., Krieger, K., Sommer, D., Schwarzbach, M., Laiacker, M., Kossyk, I., Parusel, S., Haddadin, S., and Albu-Schaffer, A. (2013). First analysis and experiments in aerial manipulation using fully actuated redundant robot arm. In *Intelligent Robots and Systems (IROS), 2013 IEEE/RSJ International Conference on*, pages 3452–3457. IEEE.

Jiang, G. and Voyles, R. (2013). Hexrotor uav platform enabling dextrous aerial mobile manipulation. In *International Micro Air Vehicle Conference and Competitions (SSRR), Linkoping, Sweden, Oct*, pages 21–26.

Jimenez-Cano, A., Martin, J., Heredia, G., Ollero, A., and Cano, R. (2013). Control of an aerial robot with multi-link arm for assembly tasks. In *Robotics and Automation (ICRA), 2013 IEEE International Conference on*, pages 4916–4921. IEEE.

Keemink, A. Q., Fumagalli, M., Stramigioli, S., and Carloni, R. (2012). Mechanical design of a manipulation system for unmanned aerial vehicles. In *Robotics and Automation (ICRA), 2012 IEEE International Conference on*, pages 3147–3152. IEEE.

Kim, S., Choi, S., and Kim, H. J. (2013). Aerial manipulation using a quadrotor with a two dof robotic arm. In *Intelligent Robots and Systems (IROS), 2013 IEEE/RSJ International Conference on*, pages 4990–4995. IEEE.

Korpela, C., Brahmbhatt, P., Orsag, M., and Oh, P. (2013). Towards the realization of mobile manipulating unmanned aerial vehicles (mm-uav): Peg-in-hole insertion tasks. In *Technologies for Practical Robot Applications (TePRA), 2013 IEEE International Conference on*, pages 1–6. IEEE.

McArthur, D. R., Chowdhury, A. B., and Cappelleri, D. J. (2018a). Autonomous control of the interacting-boomcopter uav for remote sensor mounting. In *2018 IEEE International Conference on Robotics and Automation (ICRA)*, pages 1–6. IEEE.

McArthur, D. R., Chowdhury, A. B., and Cappelleri, D. J. (2018b). Design of the interacting-boomcopter unmanned aerial vehicle for remote sensor mounting. *Journal of Mechanisms and Robotics*, 10(2):025001.

Mellinger, D., Shomin, M., Michael, N., and Kumar, V. (2013). Cooperative grasping and transport using multiple quadrotors. In *Distributed autonomous robotic systems*, pages 545–558. Springer.

Michael, N., Fink, J., and Kumar, V. (2011). Cooperative manipulation and transportation with aerial robots. *Autonomous Robots*, 30(1):73–86.

Palunko, I., Cruz, P., and Fierro, R. (2012). Agile load transportation: Safe and efficient load manipulation with aerial robots. *IEEE Robotics & Automation Magazine*, 19(3):69–79.

Papachristos, C., Alexis, K., and Tzes, A. (2014). Efficient force exertion for aerial robotic manipulation: Exploiting the thrust-vectoring authority of a tri-tiltrotor uav. In *Robotics and Automation (ICRA), 2014 IEEE International Conference on*, pages 4500–4505. IEEE.

Pexel (2018). Copyright-free images available on. `www.pexels.com`.

Pounds, P. E., Bersak, D. R., and Dollar, A. M. (2011a). Grasping from the air: Hovering capture and load stability. In *Robotics and Automation (ICRA), 2011 IEEE International Conference on*, pages 2491–2498. IEEE.

Pounds, P. E., Bersak, D. R., and Dollar, A. M. (2011b). The yale aerial manipulator: grasping in flight. In *Robotics and Automation (ICRA), 2011 IEEE International Conference on*, pages 2974–2975. IEEE.

Ruggiero, F., Lippiello, V., and Ollero, A. (2018). Aerial manipulation: A literature review. *IEEE Robotics and Automation Letters*, 3(3):1957–1964.

Ryll, M., Muscio, G., Pierri, F., Cataldi, E., Antonelli, G., Caccavale, F., and Franchi, A. (2017). 6d physical interaction with a fully actuated aerial robot. In *2017 IEEE International Conference on Robotics and Automation*.

Scholten, J. L., Fumagalli, M., Stramigioli, S., and Carloni, R. (2013). Interaction control of an uav endowed with a manipulator. In *Robotics and Automation (ICRA), 2013 IEEE International Conference on*, pages 4910–4915. IEEE.

Suarez, A., Soria, P. R., Heredia, G., Arrue, B. C., and Ollero, A. (2017). Anthropomorphic, compliant and lightweight dual arm system for aerial manipulation. In *Intelligent Robots and Systems (IROS), 2017 IEEE/RSJ International Conference on*, pages 992–997. IEEE.

Wopereis, H. W., Hoekstra, J., Post, T., Folkertsma, G. A., Stramigioli, S., and Fumagalli, M. (2017). Application of substantial and sustained force to vertical surfaces using a quadrotor. In *2017 IEEE International Conference on Robotics and Automation (ICRA)*, pages 2704–2709. IEEE.